International Journal of Innovative
Computing, Information and Control
Volume **9**, Number **5**, May **2013**

ICIC International ©2013 ISSN 1349-4198
pp. 1971–1986

COMPARATIVE STUDY OF CAMERA CALIBRATION MODELS FOR 3D PARTICLE TRACKING VELOCIMETRY

Basanta Joshi[1], Kazuo Ohmi[2] and Kazuo Nose[2]

[1]Graduate School of Engineering
[2]Faculty of Engineering
Osaka Sangyo University
Daito–shi, Osaka 574–8530, Japan
joshi_basanta@hotmail.com; {ohmi; nose}@osaka-sandai.ac.jp

Received April 2012; revised July 2012

Abstract. *Camera calibration is just an entry process but eventually an essential part of every particle image based velocity measurement technique. In the present paper, three representative camera calibration models are tested and their accuracy is compared for the use in the 3D particle tracking velocimetry (PTV). The three camera calibration models, proposed respectively by Hall, Tsai and Soloff, are first employed for determining their respective camera parameters based on the captured images of calibration marker points. Then they are further exploited for reconstructing the 3D coordinates of micro size particles based on their captured images by the calibrated cameras. The calibration marker points and the micro size particles are captured by two or three stereoscopic cameras with and without optical distortion, whereby the effect of different camera calibration models on the accuracy of the final reconstructed coordinates is investigated. Specific features of every camera calibration model are discussed in some detail.*

Keywords: Particle image velocimetry, Particle tracking velocimetry, Flow measurement, Camera calibration, Nonlinear least squares method

1. **Introduction.** Nowadays the particle image based velocity measurement technique has been widely accepted as a powerful flow diagnostic tool in many engineering fields. Not only in the fluid engineering applications but also in the civil engineering, architectural engineering, chemical and nuclear engineering, bio-mechanical engineering, micro-nano engineering and medical engineering applications, the whole-field velocity measurement resulting from the particle image velocimetry (PIV) or particle tracking velocimetry (PTV) offers a highly useful information about the mechanism of the flow to be investigated [1]. As the significance of the particle image based measurement approach is increased in the flow diagnosis experiments and the measurement is performed more often in 3D than in 2D, the accuracy of the flow velocity recovered from the particle images has become a critical issue of the measurement technique. The accuracy is all the more important, because many other derivative quantities (drag, lift, pressure, oscillation frequency, etc.) of the flow can be numerically calculated from the particle image based velocity results [2]. In particular, in the case of the latest technology of 3D PIV or PTV, where the tomographic reconstruction technique is used for locating a large number of 3D particle images [3], the accuracy is more sensitively influenced by the calibration scheme of the cameras capturing the particle images to be analyzed. A slightest error in the camera calibration parameters may result not only in the mis-location of the reconstructed particle images but even in the mis-identification of the presence of particles.

From such a background, the present authors have been concerned with the camera calibration models and the numerical schemes of calculating the calibration parameters

for the use in the 3D PTV [4]. This PTV technique tries to recover the flow velocity by tracking the movement of individual particles in the fluid, so that the mis-location or mis-identification of particles is a more critical issue than in the PIV technique that tracks the motion of the ensemble of particles. In the camera calibration, the task requires the computation of an accurate metric from the captured images and determines the parameters which maps the 3D coordinates of a certain point into their corresponding 2D projections onto the image plane of the camera. The calibration of a pinhole based perspective camera amounts to find a linear mapping function in the projective space. In this context, the direct mapping scheme with the principle of 3D affine transformation developed by Hall et al. [5] is a widely accepted linear calibration method. Obviously, this type of linear model is advantageous from the viewpoint of simplicity and computational stability.

However, most of the real camera systems cannot be fully described by this linear pinhole model because any objective lens of the camera systems has to exhibit nonlinear optical distortion. Especially with the cameras obliquely viewing the arrangement of objects, the calibration procedure requires higher order nonlinear mapping functions to precisely transform the image pixels to the 3D physical space coordinates. In this respect, there are many well established camera calibration models that are based on the combination of the 3D affine transformation and the nonlinear perspective transformation, among which the most often cited models are Faugeras and Toscani [6], Tsai [7] and Weng et al. [8]. Some other new methods to compensate the nonlinear optical distortion have been developed by Zhang [9] and Jin et al. [10] in recent years and a comparative study of some of these methods has been carried out by Salvi et al. [11].

On the other hand, the camera calibration in the PIV or PTV techniques has been often treated as a geometrical reconstruction process without need for complete knowledge of the optical system geometry. In this context, Soloff et al. [12] use a calibration target plate with a regularly spaced grid of marks printed on it. While moving the target plate by a specified amount in the out-of-plane direction (z-axis), the camera images are captured typically at 3 to 7 depth positions. In this case, the mapping function is composed of third-order polynomials in the x and y directions but only second-order ones in z direction. According to this principle, this nonlinear calibration technique basically makes use of coplanar target points, which stands in contrast to the above-mentioned geometrical optics based techniques that can work with not only coplanar but also non-coplanar target points. The advantage of the polynomial function model is that the whole mapping procedures are integrated in a purely mathematical process so that no reflection of the optical geometry is required. However, this last point turns out to be also a negative aspect of the polynomial model because almost no feedback can be expected from the optical geometry to the calculated camera parameters.

In this context, there have been studies done on the camera calibration for particle image based measurement techniques but most of them focused on the application to the cross-correlation PIV [13, 14, 15]. There have been few studies concerning the calibration schemes for the use in PTV. Although there are some accuracy oriented studies in the case of stereoscopic PTV [16, 17, 18], the calibration method itself has not been investigated thoroughly.

So in the present work, three representative and most popular calibration methods are selected from each category of camera calibration models and their performance is investigated from the viewpoint of practicability in the application to the PTV measurement. The first one is the simple pinhole based linear mapping method [5] (referred to as Hall model hereafter), which is basically derived from the linear perspective transform

formulation combined with the 3D affine transformation. In this basic camera calibration model, there are 11 camera parameters to be determined by a linear least squares calculation. The second one is the famous Tsai's nonlinear camera model [7], in which 5 internal (intrinsic) and 6 external (extrinsic) parameters must be determined by a nonlinear least squares calculation. The last one is the Soloff's nonlinear polynomial model [12], in which 38 camera parameters should be estimated by a nonlinear least squares calculation. Theoretically, the last two nonlinear models are supposed to describe more properly the optical distortion of the camera systems but in reality, they are more sensitively influenced by the number and precision of the calibration target points as well as by the numerical schemes used in the nonlinear least squares calculation. So there is no guarantee that the accuracy of the nonlinear models should always outperform that of the linear model in the practical PTV measurement.

With such a consideration, in the present work, the performance of the three camera calibration models is investigated on the basis of undistorted and distorted images of the coplanar calibration points which are widely employed in the PIV/PTV measurement and of the micro particles seeded (suspended) in the calibrated measurement volume. The camera images of calibration points and micro particles are first produced synthetically by computer simulation and then experimentally by two or three stereoscopic cameras viewing planar calibration points. The performance itself is evaluated in terms of the accuracy of the 3D reconstructed coordinates of the calibration points themselves or of those of the micro particles. A special care is taken while detecting and locating the markers position by using proper image segmentation methods. Some discussions about the applicability of each camera calibration model will be made in some detail.

2. **Camera Calibration Technique.**

Generally, the camera calibration is divided into two steps. The first step, or the camera modeling, deals with the mathematical approximation of the physical and optical behavior of the system by using a set of camera parameters. The second step deals with the use of direct or iterative numerical methods to estimate the values of these camera parameters, which is often called "calibration" in a narrow sense. The camera modeling depends on two types of camera parameters: one is the extrinsic (external) parameters which define the position and orientation of the camera in the scene with respect to the world coordinate system, and the other is the intrinsic (internal) parameters which describe the internal geometry of the camera, i.e., the effective focal length of the camera, the lens distortion coefficients and the coordinates of the optically principal point [11].

2.1. **Generalized camera modeling.**

In a standard pinhole based perspective camera, the geometrical relationship between a 3D point in the world coordinate system and its 2D projection in the camera coordinate system can be illustrated as in Figure 1. In this figure, WCS, CCS and ICS refer to the world coordinate system, the camera coordinate system and the image coordinate system respectively. The transformation from the world coordinate system P_w to the camera coordinate system P_c is given by Equation (1) or, more specifically, by Equation (2) in which the two 3D coordinate systems (P_w and P_c) and the rotation and translation matrices (R and T) are expressed with their own components.

$$P_c = RP_w + T \tag{1}$$

$$\begin{pmatrix} X_c \\ Y_c \\ Z_c \end{pmatrix} = \begin{pmatrix} r_{11} & r_{12} & r_{13} \\ r_{21} & r_{22} & r_{23} \\ r_{31} & r_{32} & r_{33} \end{pmatrix} \begin{pmatrix} X_w \\ Y_w \\ Z_w \end{pmatrix} + \begin{pmatrix} T_x \\ T_y \\ T_z \end{pmatrix} \tag{2}$$

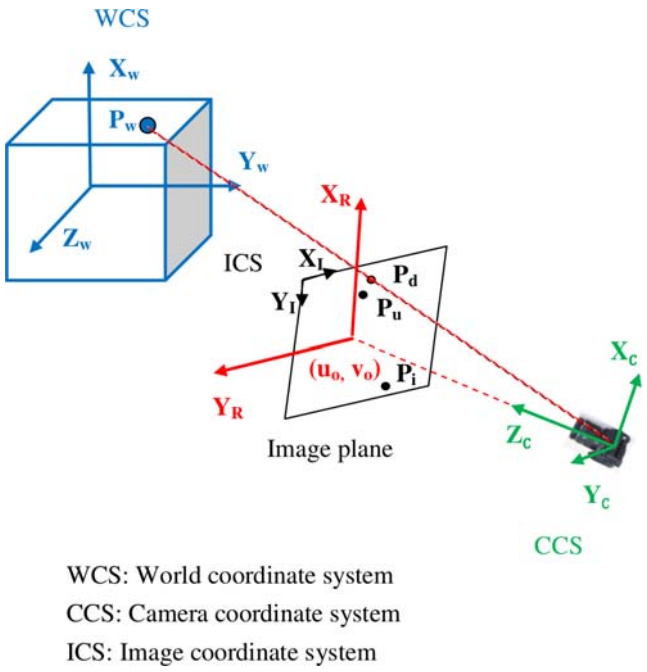

FIGURE 1. Schematic illustration of the generalized camera calibration

More precisely, the rotation matrix R in Equation (2) can be expressed by three Euler angles: yaw α, pitch β and tilt γ as shown below.

$$R = \begin{pmatrix} \cos\gamma\cos\alpha & \sin\gamma\cos\alpha & -\sin\alpha \\ -\sin\gamma\cos\beta + \cos\gamma\sin\alpha\cos\beta & \cos\gamma\cos\beta + \sin\gamma\sin\alpha\sin\beta & \cos\alpha\sin\beta \\ \sin\gamma\sin\beta + \cos\gamma\sin\alpha\cos\beta & -\cos\gamma\sin\beta + \sin\gamma\sin\alpha\cos\beta & \cos\alpha\cos\beta \end{pmatrix} \quad (3)$$

The camera coordinates $P_c(X_c, Y_c, Z_c)$ and the undistorted image coordinates $P_u(x_u, y_u)$ are related by the following perspective transformation:

$$\left.\begin{aligned} x_u &= f\frac{X_c}{Z_c} \\ y_u &= f\frac{Y_c}{Z_c} \end{aligned}\right\} \quad (4)$$

where f is the effective focal length of the lens system. The optical distortion of the real lens systems generates a distorted image point $P_d(x_d, y_d)$ with respect to the undistorted point $P_u(x_u, y_u)$ according to the following relation:

$$\left.\begin{aligned} x_d &= x_u + \delta_x \\ y_d &= y_u + \delta_y \end{aligned}\right\} \quad (5)$$

Specifically, the optical distortion involves both radial and tangential distortion, which grows with the distance from the center of the optical axis as follows:

$$\left.\begin{aligned} \delta_{xr} &= x_u\left(k_1 r^2 + k_2 r^4 + \ldots\right) \\ \delta_{yr} &= y_u\left(k_1 r^2 + k_2 r^4 + \ldots\right) \end{aligned}\right\} \quad (6)$$

$$\left.\begin{aligned} \delta_{xt} &= \varepsilon_1\left(r^2 + 2x_u^2\right) + 2\varepsilon_2 x_u y_u \\ \delta_{yt} &= \varepsilon_2\left(r^2 + 2y_u^2\right) + 2\varepsilon_1 x_u y_u \end{aligned}\right\} \quad (7)$$

where k_1 and k_2 are the radial distortion and ε_1 and ε_2 are the tangential distortion coefficients. The radius r is given by

$$r = \sqrt{x_d^2 + y_d^2} \tag{8}$$

Finally, the point in the real image coordinate system $P_i(x_i, y_i)$ can be obtained from that in the distorted image coordinate system $P_d(x_d, y_d)$ by using the coordinates of the projection center $P_0(x_0, y_0)$ and the image scale factor $s(s_x, s_y)$ in x and y directions.

$$\left.\begin{aligned} x_i &= s_x x_d + x_0 \\ y_i &= s_y y_d + y_0 \end{aligned}\right\} \tag{9}$$

2.2. **Calibration schemes.** Among the calibration schemes tested in the present work, the simplest linear calibration model of Hall [5] is approximated by means of a transformation matrix as shown in Equation (10), which is the direct combination of Equations (2), (4) and (5) by neglecting the distortion parameters δ_x and δ_y. A_{34} of this model is a global scaling factor and regarded as unity. The rest of 11 parameters are determined using a least squares technique.

$$\begin{pmatrix} x_u \\ y_u \\ 1 \end{pmatrix} = \begin{pmatrix} A_{11} & A_{12} & A_{13} & A_{14} \\ A_{21} & A_{22} & A_{23} & A_{24} \\ A_{31} & A_{32} & A_{33} & A_{34} \end{pmatrix} \begin{pmatrix} X_w \\ Y_w \\ Z_w \\ 1 \end{pmatrix} \tag{10}$$

By contrast, the nonlinear calibration techniques include different kinds of lens distortion factors in the camera model. These methods are supposed to offer a more accurate solution but computationally intensive and require good initial estimates [19]. The camera parameters are usually obtained by an iterative numerical calculation and the accuracy of calibration usually increases by repeating the iterations up to a convergence. A typical nonlinear model of Soloff [12] based on a polynomial mapping function is described as follows.

$$\begin{aligned} x_i = {} & a_0 + a_1 X_w + a_2 Y_w + a_3 Z_w + a_4 X_w^2 + a_5 X_w Y_w + a_6 Y_w^2 + a_7 X_w Z_w \\ & + a_8 Y_w Z_w + a_9 Z_w^2 + a_{10} X_w^3 + a_{11} X_w^2 Y_w + a_{12} X_w Y_w^2 + a_{13} Y_w^3 \\ & + a_{14} X_w^2 Z_w + a_{15} X_w Y_w Z_w + a_{16} Y_w^2 Z_w + a_{17} X_w Z_w^2 + a_{18} Y_w Z_w^2 \end{aligned} \tag{11}$$

$$\begin{aligned} y_i = {} & b_0 + b_1 X_w + b_2 Y_w + b_3 Z_w + b_4 X_w^2 + b_5 X_w Y_w + b_6 Y_w^2 + b_7 X_w Z_w \\ & + b_8 Y_w Z_w + b_9 Z_w^2 + b_{10} X_w^3 + b_{11} X_w^2 Y_w + b_{12} X_w Y_w^2 + b_{13} Y_w^3 \\ & + b_{14} X_w^2 Z_w + b_{15} X_w Y_w Z_w + b_{16} Y_w^2 Z_w + b_{17} X_w Z_w^2 + b_{18} Y_w Z_w^2 \end{aligned} \tag{12}$$

As a results of this formulation, this Soloff model requires a total of 38 camera parameters to be determined for each camera. This type of polynomial function based calibration model is rather robust and accurate if a sufficient number of calibration target points are provided. A by-product of this a bit elaborate manipulation is a large number of parameters not all of which are statistically relevant as pointed out by Wieneke [13].

On the other hand, for computer vision applications, different types of nonlinear calibration models based on the geometrical optics are preferred because of the possibility of the use of both coplanar and non-coplanar calibration targets. But in such applications, there are usually no approximate solutions of extrinsic or intrinsic parameters known a-priori. To circumvent this problem, one common strategy is to divide the camera calibration process into two steps [7, 8]. The first step tries to generate approximate estimates of as many parameters as possible using a linear least squares technique. In the second step, the rest of the parameters are obtained using a nonlinear optimization

method that finds the best fit between the approximately determined image points and those predicted by the mapping function. But the approximate solutions provided by the linear techniques must be good enough for the subsequent nonlinear optimization to properly converge. As expected from the above scenario, this type of two step method incorporates lens distortion in the second step of parameter estimation. In that step, the higher order radial and tangential distortions can be neglected depending on the quality of the lens systems which in turn reduces the parameters to be estimated.

In the case of the typical two step calibration method of Tsai [7], the intrinsic and extrinsic parameters to be determined in the first step are s_x, all the components of matrix R and the first two components of matrix T (T_x and T_y). Another scaling factor s_x is assumed to be unity. Then the focal length f and the last component of matrix T (T_z) are also estimated in this first step. Both of these computations can be done by solving a linear system equation. Next, in the second step, the optimal value of the radial distortion factor k_1 (neglecting the second order or higher radial distortion and all the tangential distortion terms) is searched for by simultaneously solving Equations (2), (4) and (5), while the tentative estimates of f and T_z are iteratively adjusted. To do this search, a nonlinear system equation must be solved and, depending on the scheme of the nonlinear optimization, the solutions may exhibit computational instability. Finally, all the parameters are further refined by using generalized equations for nonlinear calibration in Equations (13) and (14) which can be obtained by combining Equations (2), (4), (5), (6) and (7).

$$\left.\begin{aligned} x_u &= \frac{r_{11}X_w + r_{12}Y_w + r_{13}Z_w + T_x}{r_{11}X_w + r_{12}Y_w + r_{13}Z_w + T_z} \\ y_u &= \frac{r_{21}X_w + r_{22}Y_w + r_{23}Z_w + T_y}{r_{11}X_w + r_{12}Y_w + r_{13}Z_w + T_z} \end{aligned}\right\} \tag{13}$$

$$\left.\begin{aligned} x_d &= x_u + x_u\left(k_1 r^2 + k_2 r^4\right) + \varepsilon_1\left(r^2 + 2x_u^2\right) + 2\varepsilon_2 x_u y_u \\ y_d &= y_u + y_u\left(k_1 r^2 + k_2 r^4\right) + \varepsilon_2\left(r^2 + 2y_u^2\right) + 2\varepsilon_1 x_u y_u \end{aligned}\right\} \tag{14}$$

It should be noted that the positions of the distorted and undistorted 2D coordinates in Equation (14) are inverted from the original expression by Tsai. This is for the sake of simplicity in the numerical calculation process.

3. **Results and Discussions.**

3.1. **Test data.** In the first part of experiment, the performance of the three calibration schemes (Hall, Soloff and Tsai) are investigated by using the synthetic particle images of the PIV Standard Image project of Visualization Society of Japan [20]. This is a comprehensive set of time-series particle images showing a motion of an impinging jet in a cavity and often used by the PIV/PTV researchers as a benchmark of particle images [16, 21]. In the library of the 3D standard image [20], time-series particle images with three different viewing angles are provided with their respective calibration target images, which are composed of very small size white points almost similar to the particles in the PIV/PTV images. Out of these sets of standard images, the user first calculates the camera parameters, depending on the camera calibration model used, and then try to reconstruct the 3D coordinates of the individual particles in the time series images. Finally the motion of each reconstructed particle is tracked during the duration of the time series data. All these reconstructed data of coordinates and velocities can be directly compared to the theoretical values and thereby, the accuracy of the PTV measurement is estimated.

Four different series of standard images namely #351, #352, #371 and #377 were taken for the present test. The camera viewing angles are different from series to series as specified. In the first two series (#351 and #352) of 3D images, the observation volume is viewed from three different angles, which are $-30°$, $0°$ and $30°$ with respect to the vertical axis which is normal to the illumination. Since the two series capture the same motion of flow at the same position of observation volume, same calibration target image is used common to both cases. The only difference is the number (density) of particles seeded in the volume. In the third series (#371), the observation volume is half reduced and the camera viewing angles are also slightly changed from #351 and #352. While the optical axes of the three cameras in #351 and #352 lie in the same plane normal to the illumination, those of #371 are tilted with respect to that plane. The tilt angles are $-10°$, $20°$ and $-10°$ respectively. In the last series (#377), the observation volume is another half reduced and the camera viewing angles become much more complicated. The three viewing angle of the three cameras are $0°$, $-90°$, $30°$; $-30°$, $-45°$, $-15°$; and $-30°$, $-45°$, $15°$. Typical camera images of calibration target points and of seeded particles in series #352 are given in Figures 2 and 3. All of these images have a 256×256 pixel resolution.

One important modification made in the original calibration images is the addition of a new calibration point at each intermediate position between every two adjacent calibration points. This addition of intermediate calibration points is carried out only in x and y directions because the polynomial mapping function of the Soloff calibration model does not resolve the third order distortion in z direction. As a result, each calibration target image is composed of $5 \times 5 \times 3$ marker points in the cubic arrangement. The interval of

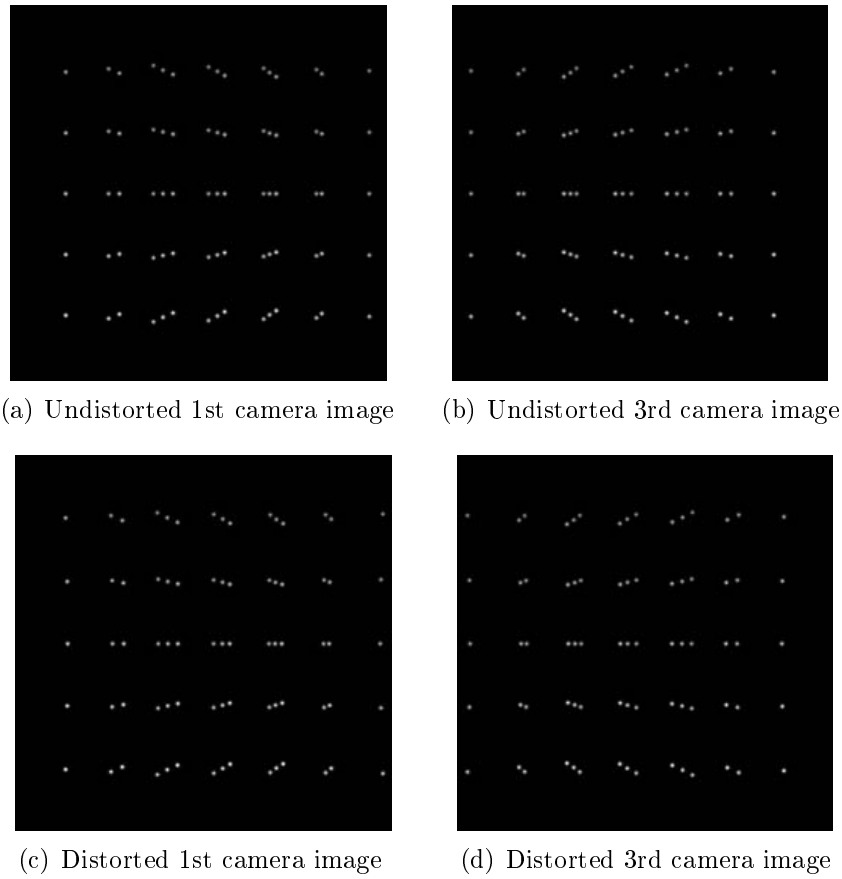

(a) Undistorted 1st camera image (b) Undistorted 3rd camera image

(c) Distorted 1st camera image (d) Distorted 3rd camera image

FIGURE 2. Calibration points of the standard image #352

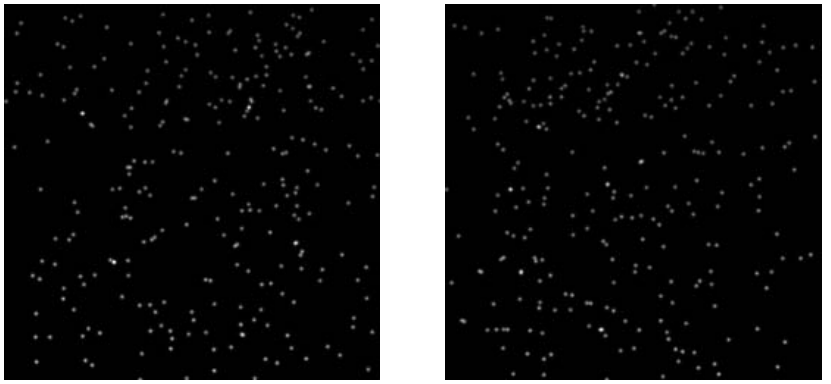

(a) Undistorted 1st camera image (b) Undistorted 3rd camera image

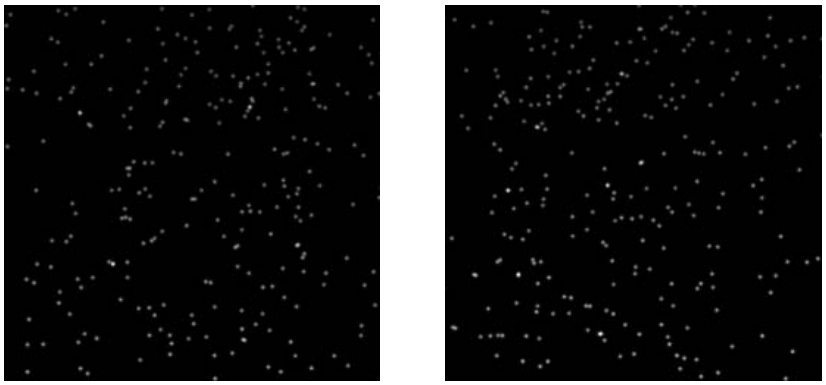

(c) Distorted 1st camera image (d) Distorted 3rd camera image

FIGURE 3. Seeded particles of the standard image #352

the marker points in the world coordinate system is 4 mm in x and y directions but 8 mm in z direction.

Although the standard image data take into account the refraction effect at the water/air interface present between the camera and the calibration target (or the particles), they do not include the distortion effect of the camera lens system which is one of the major influential factors on the accuracy of the reconstructed 3D coordinates. To simulate such a distortion effect in the real PTV experiments, all the particle images and the calibration target images of the PIV Standard Image are radially distorted as well as weakly tilted with respect to the reference observation plane of the calibration points. The radial distortion simulates that of the real lens system and the weak tilting angle corresponds to a small degree of misalignment in the setup of camera optics. Several sets of calibration point images and actual particle images are simulated based on the standard image #352 by introducing different factors of distortion and tilt and thereby the performance check is carried out regarding the reconstructed 3D particle coordinates. The first-order and second-order radial and tangential distortions are taken into consideration in this simulation which is summarized in Table 1.

In the second part of experiment, the performance of the three calibration schemes are examined by using two sets of experimental images of calibration points. All the images were captured in a small rectangular cavity ($170\times30\times180$ mm^3) with water as in the case of the real PTV experiment. The light source was a laser light flux with a rectangular cross section which illuminated only the inside of cavity. Two CCD cameras in stereoscopic arrangement captured the images of a calibration plate placed in the cavity. Each CCD cameras (JAI CM-140GE) was equipped with either a telecentric lens (Edmund TS Silver

TABLE 1. Distortion parameters applied to the standard image #352

Case	$k_1(\times 10^{-6})$	$k_2(\times 10^{-11})$	$\varepsilon_1(\times 10^{-8})$	$\varepsilon_2(\times 10^{-11})$	$s_x(\times 10^{-5})$
I	0	0	0	0	0
II	2.90	–2.20	0	0	0
III	2.90	–2.20	2.90	–2.20	0
IV	2.90	–2.20	2.90	–2.20	5.50
V	3.50	–2.60	2.90	–2.20	5.50

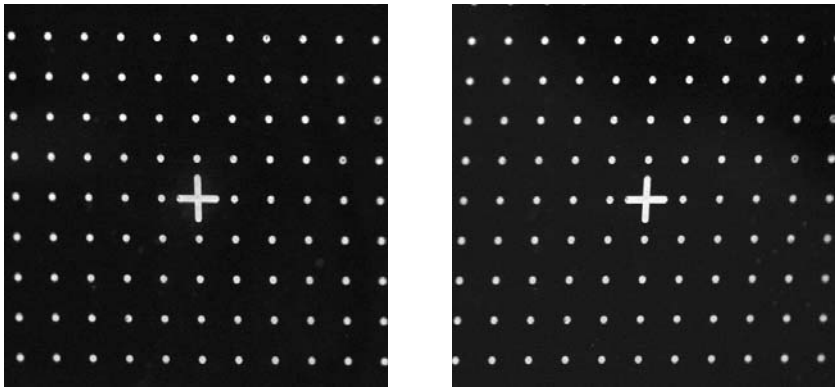

(a) Left camera image (b) Right camera image

FIGURE 4. Calibration point images captured by a telecentric lens.

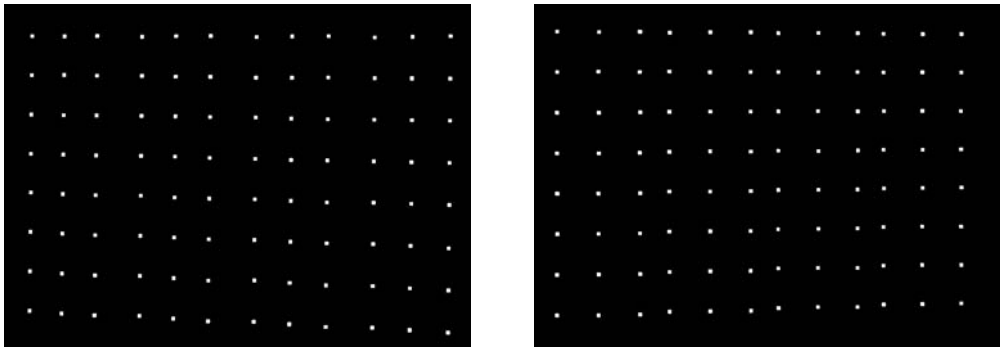

(a) Left camera image (b) Right camera image

FIGURE 5. Calibration point images captured by an ordinary objective lens.

0.2×) or an ordinary objective lens (Nikon AiAF 50 mm f/1.4D). The use of the telecentric lens can minimize the optical distortion effect, while the ordinary objective lens is not free from optical distortion. With the telecentric lens, the cameras captured images of a calibration plate with fine dot pattern (2.5 mm interval in x and y directions) at three depth positions, while with the ordinary lens, they were aimed at a calibration plate with rather rough dot pattern (10 mm interval in x and y directions). This difference in the dot pattern is due to the different magnifying factor of the two lens systems and the effective number of calibration points captured by the two systems is similar (90 versus 96). The captured images of the calibration points by two systems are shown in Figures 4 and 5.

3.2. **Numerical schemes.** On the basis of these synthetic and experimental particle image data, the first step analysis is to estimate the camera calibration parameters from the locations of the calibration points in the camera image coordinate system $(x_i,\ y_i)$

and those in the world coordinate system (X_w, Y_w, Z_w). Since in any camera calibration model, there are only two mapping equations available from one single calibration point, there must be at least half as many calibration points as the number of the unknown camera parameters. In the case of the present calibration target images, the total number of the captured calibration points is between 75 and 96, indicating that the Hall camera parameters can be calculated from 13.6 to 17.5 times as many equations, the Soloff parameters from 3.9 to 5.1 times as many equations and the Tsai parameters from 13.6 to 17.5 times as many equations. This type of simultaneous equations are usually solved approximately by using a linear least squares calculation (pseudo-inverse matrix calculation). So in the present study, the Hall and Soloff camera parameters as well as the Tsai camera parameters in the first step calibration are calculated by this scheme. Only the second step Tsai parameters must be determined by using another nonlinear optimization scheme as described below.

Once the camera calibration parameters are determined, the next step is to reconstruct the 3D coordinates of the calibration points themselves as well as of the seeded particles. Then the comparison is made between the reconstructed coordinates and the known (theoretical) coordinates. In order to reconstruct the 3D coordinates of a point in the world coordinate system, the 2D image coordinates of the same point from at least two camera views are needed. In reality, if there are two camera views of a single point, that makes four simultaneous equations with three unknown variables X_w, Y_w, Z_w. If there are three camera views, six simultaneous equations for three unknowns. This problem can be solved again by using a linear least squares calculation (pseudo-inverse matrix calculation) in the case of the Hall linear model. The same scheme can be applied to the Tsai nonlinear model because in his model, once the camera parameters are determined, the mapping relation between the world coordinate system and the image coordinate system becomes linear. But in the present study, to reconstruct the 3D coordinates of particles by the Tsai model, other types of nonlinear least squares optimization methods are used in stead of the linear method because of the numerical instability of the inverse matrix to be calculated in the linear least squares system. More precisely, the Gauss-Newton algorithm or the Levenberg-Marquardt algorithm [22] is selectively used depending on the reconstruction error with respect to the predicted values by the Hall model.

In the last case of the Soloff model, the linear least squares calculation cannot be applicable to reconstruct the 3D coordinates because the mapping functions are nonlinear polynomials. So the Levenberg-Marquardt algorithm [22] is again used to determine the 3D coordinates of particles. To solve the nonlinear least squares equations either by the Gauss-Newton algorithm or the Levenberg-Marquardt algorithm, the Jacobian and Hessian matrices must be calculated. The partial derivatives to be used for these matrices are estimated by the 5th order finite difference approximation. Then, iteration is carried out to get to the optimal solutions starting from proper initial values. To guarantee the convergence of the solutions, an initial guess of the 3D coordinates is given by the Hall calibration model.

The accuracy of the tested calibration models is ascertained by estimating the discrepancy of particle 3D coordinates P_w between the reconstructed results and the pre-known theoretical values. This discrepancy, or the error E, is calculated by the Euclidean distance of the reconstructed (X_w, Y_w, Z_w) and theoretical (X'_w, Y'_w, Z'_w) 3D coordinates as shown below:

$$E = \sqrt{(X_w - X'_w)^2 + (Y_w - Y'_w)^2 + (Z_w - Z'_w)^2} \tag{15}$$

3.3. **Calibration performance.** The first calibration test was carried out by using the standard image data-set of #352 with and without optical distortion. The camera parameters of each of the three calibration models were determined from the image of calibration marker points as described in the previous section. The number of camera parameters to be determined for each camera is 11 in the Hall model, 38 in the Soloff model and 11 in the Tsai model. Based on the determined camera parameters, the 3D coordinates of the same calibration marker points as used for camera calibration were reconstructed and compared with the theoretical coordinates. The results are briefly summarized in Table 2 where the mean and the standard deviation of the reconstruction errors at 75 marker points are compared in terms of five different image distortion degrees (Case I through V) and of three different camera calibration models (Hall, Soloff and Tsai).

The first observation from this table is that in the Hall model, the mean reconstruction error as well as the standard deviation are increased as higher degree of optical distortion is included in the tested calibration image. In particular, the standard deviation is drastically increased as the higher distortion is introduces. But in the Soloff model, the reconstruction error remains within an almost similar level regardless of the optical distortion. Furthermore, the error level itself is low and highly stable. Only in the Case I image, the error level is comparable to the Hall model. Finally, in the Tsai model, the general trend is again the increment of reconstruction error as the optical distortion becomes higher. The level of reconstruction error is in some cases smaller but otherwise larger than the Hall model. In general, the reconstruction error of the Tsai model is considerably fluctuant according to the experimental conditions and the accuracy is rather unstable. This is mainly due to the numerical instability of the nonlinear optimization used in the process of reconstruction.

The second calibration test was conducted by using the same standard image dataset of #352 and trying to reconstruct the 3D coordinates of the seeded particles as in the real PTV experiment. The number of seeded particles per volume in this dataset is 273, so that the output of the statistic values of reconstruction error are considered more

TABLE 2. Reconstruction error of the calibration points in the standard image #352

Case	Mean [mm]			Standard deviation [mm]		
	Hall	Soloff	Tsai	Hall	Soloff	Tsai
I	0.046	0.034	0.046	0.012	0.021	0.012
II	0.116	0.033	0.105	0.069	0.020	0.062
III	0.116	0.034	0.105	0.069	0.020	0.062
IV	0.117	0.034	0.183	0.070	0.020	0.120
V	0.137	0.034	0.140	0.084	0.019	0.094

TABLE 3. Reconstruction error of the seeded particles in the standard image #352

Case	Mean [mm]			Standard deviation [mm]		
	Hall	Soloff	Tsai	Hall	Soloff	Tsai
I	0.043	0.039	0.047	0.010	0.019	0.017
II	0.166	0.047	0.112	0.127	0.037	0.102
III	0.166	0.047	0.112	0.127	0.037	0.102
IV	0.166	0.047	0.241	0.130	0.037	0.299
V	0.199	0.049	0.079	0.157	0.041	0.075

meaningful. The results are summarized in a similar manner in Table 3. Here again, in the Hall model, the mean reconstruction error and the standard deviation are increased as higher degree of optical distortion is included. But if compared to the first test with the calibration markers, both the mean and standard deviation are considerably increased in the higher distortion images. The standard deviation is almost doubled in Case V with respect to Case I. Next in the Soloff model, the error level is still low and highly stable regardless of the the optical distortion. But the overall error level is increased by 40% if compared to the calibration marker images. Finally in the Tsai model, the general trend is again the fluctuation of reconstruction errors. The effect of the optical distortion in the particle images is rather obscured by this fluctuation of errors due to the numerical instability of the nonlinear optimization. The error level itself is not so bad compared to the Hall model. At least as far as the mean reconstruction error is concerned, the error level is not so varied between the first test with calibration markers and the second test with seeded particles.

The variation of the mean reconstruction error according to the degree of optical distortion in the first and second calibration test is graphically represented in Figure 6. As observed again from this figure, the mean reconstruction error level of the Tsai model is highly fluctuant depending not simply on the degree of optical distortion but randomly on the specific experimental conditions. By contrast, the mean error level of the Soloff model is low and highly stable, only slightly increased with the optical distortion. The mean error in the Hall model is simply increased with the optical distortion as expected from the general principle of the linear calibration model.

The mean value is not always indicative of the general trend of the detailed variation of the estimated physical quantity. In addition, the calibration points and particles are not always treated in the same way by all the calibration methods. So, the reconstruction errors of the 3D coordinates must be further checked at each position of the calibration points or the particles. For this purpose, two extreme cases out of the five sets of standard image #352 were chosen, i.e., Case I without any optical distortion and Case V with the highest degree of distortion. Figure 7 shows the variation of the reconstruction error of the seeded particles with respect to the distance from the origin of the camera image coordinate system. The variation curves of error in this figure exhibit overall ripples or fluctuations and this fluctuation increases as the location of particle is moved away from the origin. Also as seen from this figure, the reconstruction error for all the three

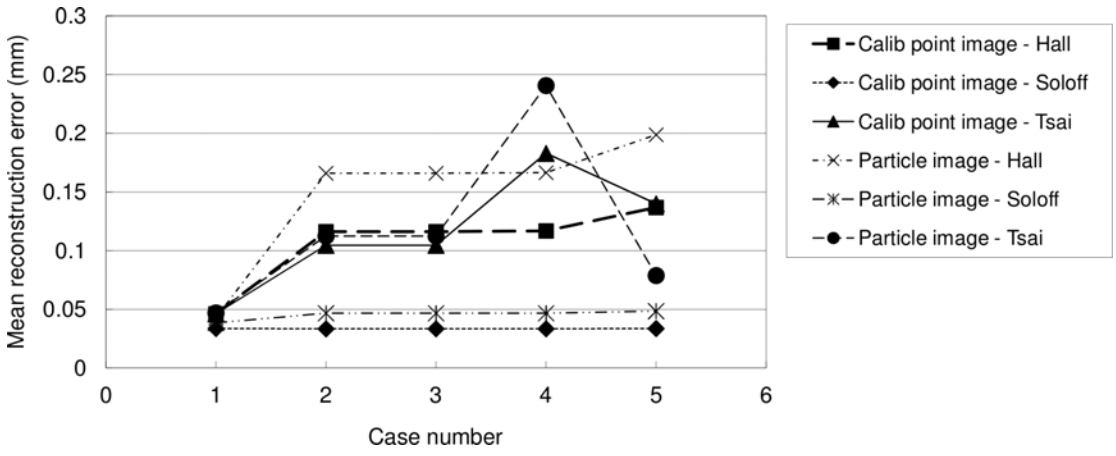

FIGURE 6. Variation of mean reconstruction error according to the optical distortion (Series #352)

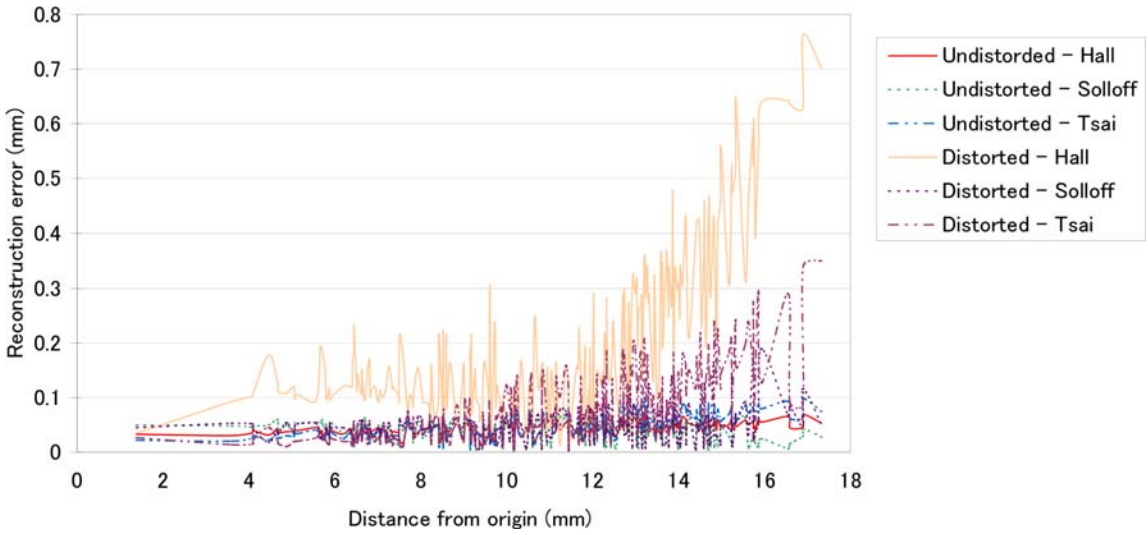

FIGURE 7. Reconstruction error for undistorted versus distorted particle images (Series #352)

TABLE 4. Reconstruction error of the seeded particles for different series of the standard image

Series No.	Undistorted image [mm]			Highly distorted image [mm]		
	Hall	Soloff	Tsai	Hall	Soloff	Tsai
351	0.042	0.038	0.046	0.167	0.046	0.225
352	0.043	0.039	0.047	0.166	0.047	0.241
371	0.012	0.056	0.015	0.080	0.035	0.644
377	0.008	0.005	0.009	0.051	0.016	0.503

calibration models is generally stable with a relatively narrow range of fluctuations in the case of the undistorted particle images (Case I), which may correspond to the mean value results shown in Table 3. By contrast, the reconstruction error in the case of the distorted particle images (Case V) is much more fluctuant, particularly so near the border area of the camera image plane. As regards the comparison of the three calibration models, the superiority of the Soloff and Tsai models over the Hall model can be clearly seen at most of the particle locations in the case of the distorted particle image. The error range in the Hall model is significantly increased if the particle is located far away from the origin and the error fluctuation goes up to a level of 0.8 mm.

In the final calibration test with the standard images, the particle images of four different data sets (Series #351, #352, #371 and #377) were selected with the highest degree of image distortion (i.e., the Case V distortion). And similarly to the first and second tests, the mean reconstruction error and the standard deviation were estimated for the three different calibration models. The main objective of this last test is to check the effect of the orientation of cameras as well as the effect of the varied arrangement of marker points on the calibration target. The results of the reconstruction error are summarized in Table 4. From this table, it is observed that the reconstruction error decreases even though the complexity of the camera arrangement was increased for the last two image data sets. It is probably due to the fact that there are a comparatively small number of particles concentrated in a thin observation volume in the case of Series #371 and #377 compared to Series #351. In the case of Series #377, another influential factor is the

TABLE 5. Reconstruction error of the calibration points in the experimentally captured image

Calibration scheme	Telecentric lens [mm]			Ordinary lens [mm]		
	Mean	Standard deviation	Max	Mean	Standard deviation	Max
Hall	0.014	0.007	0.047	0.077	0.031	0.172
Soloff	0.009	0.006	0.044	0.066	0.030	0.178
Tsai	0.014	0.007	0.048	0.540	0.222	1.122

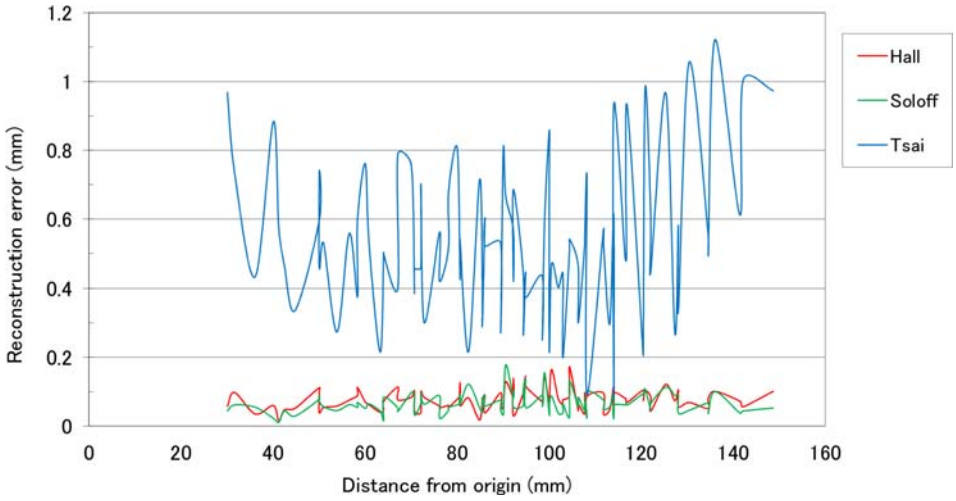

FIGURE 8. Variation of the reconstruction error in the experimentally captured image with optical distortion

arrangement of the calibration points at five depth positions as compared to the other cases with calibration points at only three depth positions.

After the performance test using the synthetic images of calibration points and particles, the accuracy of the three camera calibration models was further investigated by using the experimentally captured images of calibration points with and without optical distortion. At first, the captured images were processed by dynamic threshold binarization [23] and labeling schemes to extract the 2D coordinates of the individual calibration points. Although some other efficient algorithms to detect calibration marker points have been proposed by Zhou et al. [24], the above mentioned scheme worked more efficiently for extracting the individual calibration points. Based on these measured 2D coordinates and the known 3D coordinates of the calibration points, the camera parameters of each calibration model were calculated. Then the 3D coordinates of the same calibration points were reconstructed by using their 2D coordinates projected on the two camera screens. It should be noticed that this is the most realistic form of accuracy test in the case of the experimentally captured images because the 3D coordinates of seeded particles cannot be pre-determined in the measurement volume. The accuracy of reconstruction was estimated in terms of the rms error, the standard deviation and the maximal value of the reconstructed 3D coordinates. The results of this test are summarized in Table 5.

From this table it is observed, as expected, that the overall reconstruction error in the images without optical distortion (with telecentric lens) is far lower as compared to the images with optical distortion (with an ordinary lens). As regards the three camera calibration models, it is confirmed again that the Soloff method outperforms the others in nearly all the tested conditions. With this method, the rms value, the standard deviation

and the max value of the reconstruction error are lowest which may justify its applicability for the high precision PTV experiments. Here again, the reconstruction errors of the Tsai method are rather increased because of the convergence issue of the nonlinear optimization scheme.

Finally, similarly to the case of the synthetic images, the fluctuations of the reconstruction error of the 3D coordinates in the distorted images are plotted with respect to the distance from the origin of the camera image coordinate system as shown in Figure 8. This figure highlights the general trend of the accuracy of 3D coordinates in the three camera calibration models as the location of the target point is moved away from the origin and the differences in the maximum and minimum errors are clearly visible. For the images without optical distortion, the error fluctuation range is very small as indicated by the standard deviations in Table 5 and the reconstruction accuracy is almost comparable for all the three calibration models. However, for the images with optical distortion, there are many marked ripples in the fluctuation curve of the Tsai model with a fluctuation range almost 10 times larger than the other models.

4. **Conclusions.** Camera calibration is only a preliminary stage of the image analysis processes performed in the 3D PTV flow measurement. But at the same time, this is one of the most influential parts of the PTV measurement from the view point of the accuracy of recovered flow velocity. In the present study, one basic linear camera calibration model (Hall) and two nonlinear calibration models (Soloff and Tsai) were comparatively investigated in terms of the reconstruction error in the 3D coordinates of the calibration marker points as well as of the seeded particles in the measurement volume. The efficiency of the calibration models was ascertained first by analyzing the error results in the synthetic camera images and then, by analyzing the errors in the experimentally captured images. The conclusions obtained so far are summarized as follows:

(1) The error level of the linear Hall calibration model is very small and comparable to that of the nolinear models if there is no optical distortion in the captured images of the calibration marker points and the seeded particles. But if the distortion is present, the error level is considerably increased and error range is highly extended. This tendency is especially enhanced near the border area of the camera image plane.

(2) The nonlinear Soloff calibration model based on polynomial mapping functions is much more preferred in the PTV applications because the error level is almost constantly low regardless of the optical distortion in the captured images. A large number of camera parameters (38 per camera view) may be determined by using a simple linear least squares calculation but the reconstruction of the 3D coordinates of target points requires a more refined nonlinear least squares algorithm. In this process, the 3D coordinates obtained by the linear Hall model can be very suitably used as an initial guess of the solution.

(3) The nonlinear Tsai calibration model based on a two step determination of the camera geometry parameters is generally better than the linear Hall model but the reconstruction error level and the error range are randomly fluctuant depending on specific experimental conditions. This is mainly due to the numerical instability of the nonlinear optimization algorithm which must be used in both the parameter estimation and the 3D coordinates reconstruction processes. The good point about the Tsai calibration method is that it is applicable to both coplanar and non-coplanar calibration target points but that is not a critical issue in general 3D PTV applications.

(4) On the whole, there is not so much difference in the observations of the reconstruction errors between the synthetic images and the experimental images. One noteworthy point is that the linear Hall model yields appreciable reconstruction results in the actual experiment as compared to the more elaborate nonlinear models.

REFERENCES

[1] R. J. Adrian, Twenty years of particle image velocimetry, *Experiments in Fluids*, vol.39, pp.159-169, 2005.

[2] M. Raffel, C. Willert and J. Kompenhans, *Particle Image Velocimetry: A Practical Guide*, Springer, 1998.

[3] G. Elsinga, F. Scarano, B. Wieneke and B. Oudheusden, Tomographic particle image velocimetry, *Experiments in Fluids*, vol.41, pp.933-947, 2006.

[4] B. Joshi and K. Ohmi, Camera calibration models for 3D particle tracking velocimetry, *Proc. of the 15th Intern. Symp. on Applications of Laser Techniques to Fluid Mechanics*, Lisbon, 2010.

[5] E. Hall, J. Tio, C. McPherson and F. Sadjadi, Measuring curved surfaces for robot vision, *Computer*, vol.15, no.12, pp.42-54, 1982.

[6] O. D. Faugeras and G. Toscani, The calibration problem for stereo, *Proc. of the IEEE Conference on Computer Vision and Pattern Recognition*, Miami Beach, USA, pp.15-20, 1986.

[7] R. Tsai, A versatile camera calibration technique for high-accuracy 3d machine vision metrology using off-the-shelf TV cameras and lenses, *IEEE Journal of Robotics and Automation*, vol.3, no.4, pp.323-344, 1987.

[8] J. Weng, P. Cohen and M. Herniou, Camera calibration with distortion models and accuracy evaluation, *IEEE Trans. on Pattern Analysis and Machine Intelligence*, vol.14, no.10, pp.965-980, 1992.

[9] Z. Zhang, A flexible new technique for camera calibration, *IEEE Trans. on Pattern Analysis and Machine Intelligence*, vol.22, no.11, pp.1330-1334, 2000.

[10] S. Q. Jin, L. Q. Fan, Q. Y. Liu and R. S. Lu, Novel calibration and lens distortion correction of 3d reconstruction systems, *Journal of Physics: Conference Series*, vol.48, no.1, pp.359-363, 2006.

[11] J. Salvi, X. Armangue and J. Battle, A comparative review of camera calibrating methods with accuracy evaluation, *Pattern Recognition*, vol.35, no.7, pp.1617-1635, 2002.

[12] S. M. Soloff, R. J. Adrian and Z.-C. Liu, Distortion compensation for generalized stereoscopic particle image velocimetry, *Measurement Science and Technology*, vol.8, no.12, pp.1441-1454, 1997.

[13] B. Wieneke, Stereo-PIV using self-calibration on particle images, *Experiments in Fluids*, vol.39, pp.267-280, 2005.

[14] C. Willert, Assessment of camera models for use in planar velocimetry calibration, *Experiments in Fluids*, vol.41, pp.135-143, 2006.

[15] R. Giordano and T. Astarita, Spatial resolution of the stereo PIV technique, *Experiments in Fluids*, vol.46, pp.643-658, 2009.

[16] A. Sapkota and K. Ohmi, Neural network approach to stereoscopic correspondence of three-dimensional particle tracking velocimetry, *IEEJ Trans. on Electrical and Electronic Engineering*, vol.3, no.6, pp.612-619, 2008.

[17] S. P. Panday, K. Ohmi and K. Nose, An ant colony optimization based stereoscopic particle pairing algorithm for three-dimensional particle tracking velocimetry, *Flow Measurement and Instrumentation*, vol.22, no.1, pp.86-95, 2011.

[18] A. Sapkota and K. Ohmi, Error detection and performance analysis scheme for particle tracking velocimetry using fuzzy logic, *International Journal of Innovative Computing, Information and Control*, vol.5, no.12(B), pp.4927-4934, 2009.

[19] L. M. Song, M. P. Wang, L. Lu and H. J. Huan, High precision camera calibration in vision measurement, *Optics & Laser Technology*, vol.39, no.7, pp.1413-1420, 2007.

[20] K. Okamoto, S. Nishio, T. Kobayashi, T. Saga and K. Takehara, Evaluation of the 3-D PIV standard images (PIV-STD project), *Journal of Visualization*, vol.3, pp.115-124, 2000.

[21] K. Ohmi and N. Yoshida, 3-D particle tracking velocimetry using a genetic algorithm, *Proc. of the 10th International Symposium on Flow Visualization*, Kyoto, Japan, 2003.

[22] J. Nocedal and S. Wright, *Numerical Optimization*, Springer, New York, 1999.

[23] K. Ohmi and H. Li, Particle-tracking velocimetry with new algorithms, *Measurement Science and Technology*, vol.11, pp.603-616, 2002.

[24] D. Zhou, X. Wei, Q. Zhang and X. Fang, An automatic algorithm for accurately locating calibration markers on a chessboard, *International Journal of Innovative Computing, Information and Control*, vol.5, no.10(A), pp.3217-3226, 2009.